





## Tracking carrier and exciton dynamics in mixed-cation lead mixed-halide perovskite thin films

Qing Chang<sup>1,5</sup>, Di Bao<sup>1,5</sup>, Bingbing Chen<sup>2</sup>, Hongwei Hu<sup>2,3</sup>, Xiaoxuan Chen<sup>1</sup>, Handong Sun<sup>1</sup>, Yeng Ming Lam<sup>2</sup>, Jian-Xin Zhu<sup>4</sup>, Daming Zhao<sup>1</sup><sup>✉</sup> & Elbert E. M. Chia<sup>1</sup><sup>✉</sup>

Mixed-cation lead mixed-halide perovskites simultaneously possess structural stability and high power conversion efficiency. A thorough study of both carrier and exciton dynamics is needed to understand the photophysical properties that underpin its superior photovoltaic performance. By utilizing a broadband transient absorption spectroscopy, we observe the carrier and exciton dynamics in a  $\text{FA}_{0.85}\text{Cs}_{0.15}\text{Pb}(\text{I}_{0.97}\text{Br}_{0.03})_3$  (FCPIB) perovskite by simultaneously resolving the carrier and exciton contribution to the transient change of the absorption spectra, from which the carrier density and exciton oscillator strength can be determined. Our data reveal a quick and significant conversion of the photogenerated carriers to excitons, on top of the usual carrier recombination process. Moreover, the decay of carrier density shows a change of kinetics from a second-order recombination at high pump fluence to a third-order recombination at low pump fluence. Our analysis utilizes band anharmonicity, presents an independent determination of electronic temperature and quasi-Fermi energy, and reveals an interesting interplay among the processes of carrier cooling, exciton formation/decay and carrier recombination, all as a function of time after photoexcitation. Our work demonstrates the use of pump fluence as a knob to tune the relative populations of carriers and excitons in halide perovskite materials.

<sup>1</sup>Division of Physics and Applied Physics, School of Physical and Mathematical Sciences, Nanyang Technological University, Singapore 637371, Singapore.

<sup>2</sup>School of Materials Science and Engineering, Nanyang Technological University, Singapore 639798, Singapore. <sup>3</sup>Institute of Intelligent Flexible Mechatronics, Jiangsu University, 212013 Zhenjiang, China. <sup>4</sup>Theoretical Division and Center for Integrated Nanotechnologies, Los Alamos National Laboratory, Los Alamos, NM 87545, USA. <sup>5</sup>These authors contributed equally: Qing Chang, Di Bao. ✉email: [zhao0213@e.ntu.edu.sg](mailto:zhao0213@e.ntu.edu.sg); [elbertchia@ntu.edu.sg](mailto:elbertchia@ntu.edu.sg)

Lead halide perovskites exhibit properties of large absorption coefficient<sup>1,2</sup>, long and balanced electron and hole diffusion lengths<sup>3</sup>, and slow hot-carrier cooling due to hot-phonon bottleneck<sup>4</sup>, that make them excellent solar cell materials. This family of perovskites has been extensively studied in the field of photovoltaic<sup>5–10</sup>, light-emitting diodes (LEDs)<sup>11,12</sup>, and lasing<sup>13,14</sup>. Single-junction perovskite solar cells (PSCs) exhibit world-record power conversion efficiency (PCE) of up to 25.5% (see “<https://www.nrel.gov/pv/cell-efficiency.html>” for National Renewable Energy Laboratory Research Cell Record Efficiency Chart. <https://www.nrel.gov/pv/assets/pdfs/best-research-cell-efficiencies.20200406.pdf>). At the present time, mixed-halide perovskites can easily deliver high PCE over 20% and long-term stability against degradation by light, water, or air<sup>15–18</sup>, e.g., formamidinium-lead-halide-based perovskites exhibit both high-efficiency PCEs of 22.1% and long-term stability<sup>19</sup>.

Simulations of free charge fraction over the total excitation density by D’Innocenzo et al. showed that, under photovoltaic cell operating conditions (e.g., at room temperature and low excitation density), the fraction approaches one, i.e., the photo-generated excitons are fully ionized into free carriers, while the fraction decreases with increasing excitation density, indicating increasing amounts of exciton populations<sup>20</sup>. An open question is, upon photoexcitation, what happens to the photogenerated carriers—do they cool, recombine, or become excitons? Knowing the relative strengths of the processes of carrier cooling, carrier recombination and exciton formation, and their respective timescales, especially in the first few picoseconds after photoexcitation, will allow us to control and optimize the carrier and exciton populations of these perovskite materials for different applications such as solar cell or light-emitting diodes.

Pioneering transient absorption (TA) works<sup>4,21–23</sup> have uncovered key parameters, such as the time evolution of the carrier temperature after photoexcitation. However, in these reports, the time evolution of the carrier density, exciton density or bandgap have not been resolved. A proper analysis of TA spectra should yield carrier and exciton dynamics all within one self-consistent picture. In our work, we studied the FA<sub>0.85</sub>CS<sub>0.15</sub>Pb(I<sub>0.97</sub>Br<sub>0.03</sub>)<sub>3</sub> (FCPIB) perovskite and disentangled the exciton contributions from the free carrier ones by using a broadband white-light probe (1.5–2.0 eV). Our data showed that, shortly after photoexcitation, the photogenerated electrons cool to the conduction band (CB) edge, and holes to the valence band (VB) edge. Thereafter, some recombine via carrier recombination, while others become excitons. Our analysis enables us to track the time evolution of both carrier and exciton density, as well as the carrier recombination kinetics. Our work thus demonstrated the roles of both excitons and carriers in the photovoltaic properties of these FA-based perovskite materials.

## Results and discussion

**Steady-state absorption spectra.** The steady-state absorbance spectra (Fig. 1a) exhibit an absorption onset at ~1.6 eV and a monotonic increase with photon energy. These features agree with reports on the same compound<sup>24</sup> and their relatives (MAPbI<sub>3</sub>)<sup>25</sup>. Yang et al. employed a detailed model, based on Elliot’s theory<sup>26</sup>, to analyze both the steady-state and transient absorption spectra, assuming both the conduction band and valence band possess parabolic dispersion<sup>4,27</sup>. Thereafter, many works follow the same parabolic-band assumption in their fits to steady-state absorption, and subsequent transient absorption data analysis<sup>21,22</sup>.

However, Saba et al.<sup>28,29</sup> revealed that the steady-state absorption spectra should be fitted by introducing a nonparabolic

factor, especially for photon energies well above the bandgap. Accurate fits to steady-state absorption spectra are crucial in analyzing subsequent transient absorption data, since the extracted fitting parameters are fixed in fitting the photoinduced spectrum change. Here, we employ Elliot’s formula as well as introducing a nonparabolic band<sup>26,28–30</sup>, using

$$A(\hbar\omega) = A_{\text{CC}}(\hbar\omega) + A_{\text{EC}}(\hbar\omega), \quad (1)$$

where the carrier contribution (CC) term is

$$A_{\text{CC}}(\hbar\omega) = A_1 \frac{2\pi\sqrt{E_b}}{\hbar\omega} \frac{1}{\Gamma} \int_{E_g}^{\infty} \text{sech}\left(\frac{\hbar\omega - E}{\Gamma}\right) \frac{\xi(E - E_g)}{1 - \exp\left(-2\pi\sqrt{\frac{E_b}{E - E_g}}\right)} dE, \quad (2)$$

and the exciton contribution (EC) term is

$$A_{\text{EC}}(\hbar\omega) = A_2 \frac{2\pi E_b^{3/2}}{\hbar\omega} \frac{1}{\Gamma} \sum_{j=1}^{j_{\text{max}}=7} \frac{1}{j^3} \text{sech}\left(\frac{\hbar\omega - E_g + E_b/j^2}{\Gamma}\right), \quad (3)$$

where the prefactors  $A_1$  and  $A_2$  are proportional to the transition dipole moment,  $E_g$  is the bandgap,  $E_b$  is the exciton binding energy,  $(E_g - E_b/j^2)$  is the energy of the  $j^{\text{th}}$  excitonic state with  $j_{\text{max}}$  for cutoff (We chose  $j_{\text{max}} = 7$ , which is high enough to account for all the excitonic contribution to the absorption spectrum), the  $E_b^{3/2}$  in the EC term arises from the coupling between the wavefunctions of an electron and a hole<sup>31</sup>,  $\Gamma$  is the exciton bandwidth and  $\xi(E - E_g) = 1 + 10R(E - E_g) + 126R^2(E - E_g)^2$  is to account for band nonparabolicity effect with  $R$  being the nonparabolic factor<sup>29</sup>. Using the nonparabolic term described in Eq. (1) enables us to fit the data over a wide range of photon energies from 1.5 to 2 eV (see Fig. 1b). Without the nonparabolic term  $R$ , the fitting quality is poor (see Supplementary Note 1), while the spectra can be only well fit from 1.5 to 1.8 eV as shown in Fig. 1a. Including the  $R$  terms in the fitting model improves the fit quality, increases the energy range of fit, and also enables the fitting parameters to be stable with respect to a slight change in the fitting range (compare Supplementary Tables 1 and 2). A fit to the data up to 2.0 eV, shown in Fig. 1b, yields  $E_g = 1.631 \pm 0.008$  eV and  $E_b = 23 \pm 5$  meV. We then fix these extracted parameters in the fitting model to fit the subsequent transient absorption data.

**Determination of carrier temperature.** We further measured the TA spectra on FCPIB with above-bandgap (400 nm, for 2D contour plot see Supplementary Fig. 1) and resonant (770 nm) excitation. Figure 2a and 2c show the normalized TA spectra,  $\Delta A(\hbar\omega)$ , at representative time delays from 0.5 ps to 1 ns under 400-nm and 770-nm pump with a fluence of 83  $\mu\text{J}/\text{cm}^2$ . In Fig. 2a, a photoinduced absorption (PIA) observed below the bandgap at short time delays (e.g., 0.5 ps) has been attributed to the presence of additional optical transitions due to bandgap renormalization (BGR), rather than biexciton formation<sup>32</sup>. Such feature is absent in the TA spectra for 770-nm excitation. A large bleaching feature at energies above the bandgap implies excited states being occupied by photogenerated carriers and excitons. The probe photon energy dependence of the bleaching yields a photogenerated carrier energy distribution that obeys the Fermi-Dirac (FD) distribution. Under the condition of  $\hbar\omega \gg E_f^q$  (quasi-Fermi energy), the carrier distribution can be simplified to the Maxwell-Boltzmann (MB) distribution<sup>4,21</sup>, leading to the expression

$$\Delta A(\hbar\omega) = -C \exp\left(-\frac{\hbar\omega}{k_B T_e}\right), \quad (4)$$

where  $C$  is a prefactor,  $k_B$  is the Boltzmann constant, and  $T_e$  is the carrier temperature. By fitting the high-energy tail of the data (see Fig. 2a) to Eq. (4), we obtain  $T_e$  as a function of pump-probe

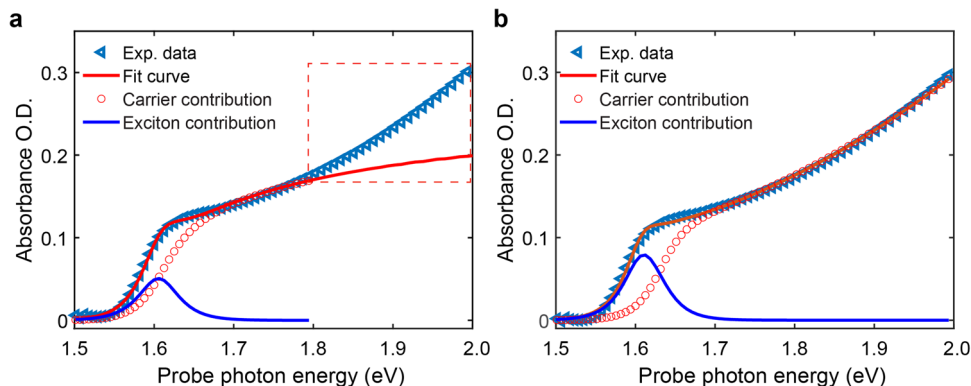


**Fig. 1 Steady-state absorption spectrum measurement.** Linear absorption spectra and fits **a** without nonparabolic and **b** with nonparabolic factor  $\xi$ . The fitting range of **a** is only from 1.5–1.8 eV. O.D. is the optical density defined by  $-\log_{10}\left(\frac{I_t}{I_0}\right)$ , where  $I_0$  is the incident optical density and  $I_t$  is the transmitted optical density.

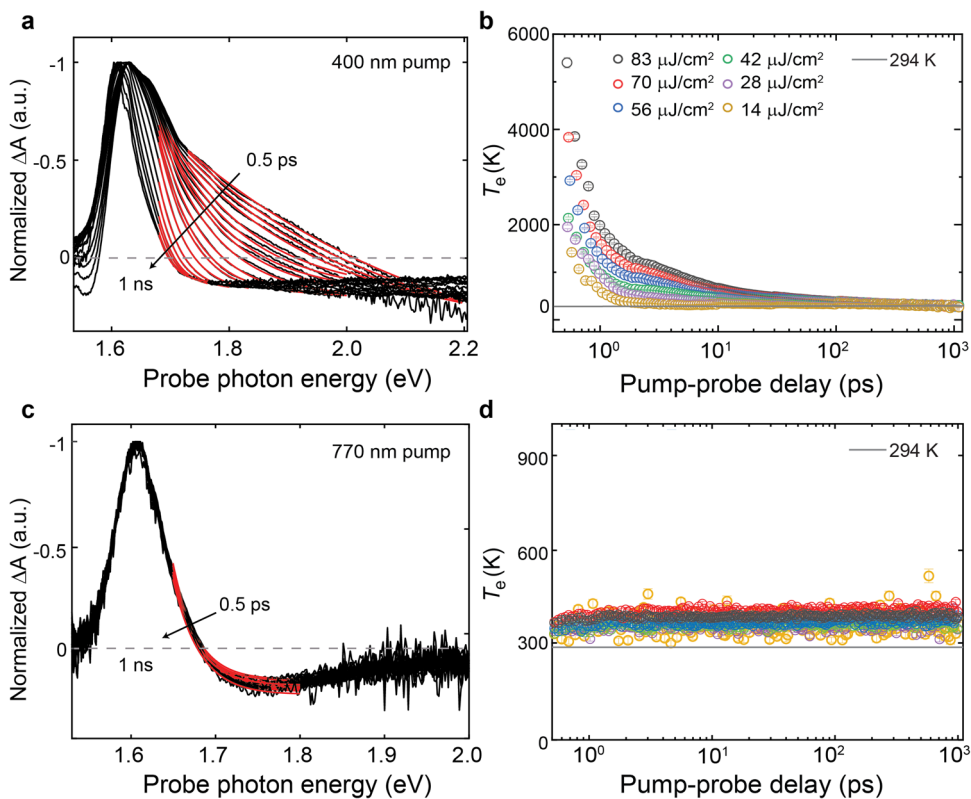


**Fig. 2 Transient absorption spectra measurements.** **a** Normalized transient absorption spectra with fluence of  $\sim 83 \mu\text{J}/\text{cm}^2$  under 400-nm pump. Red solid lines are the Maxwell-Boltzmann fit curves by using Eq. (4). **b** Extracted carrier temperatures under 400-nm at different pump fluences. **c** Normalized transient absorption spectra with fluence of  $\sim 83 \mu\text{J}/\text{cm}^2$  under 770-nm pump. **d** Extracted carrier temperatures under 770-nm pump at different pump fluences. The horizontal line marks the temperature of 294 K. Errors of  $T_e$  are standard error that is determined by calculating the 95% confidence interval, based on residual values and Jacobian matrix obtained from the fits to Eq. (4).

delay, as shown in Fig. 2b for different pump fluences. The 400-nm pump results show slow carrier cooling under high pump fluences that are consistent with previous works in this family of perovskite materials<sup>4</sup>. In contrast, the normalized  $\Delta A(h\nu)$  after 770-nm excitation shows a negligible change in the carrier temperature (Fig. 2d) by fitting the data to the MB distribution (Fig. 2c). The negligible photoinduced change in the  $T_e$  for 770-nm pump (see Fig. 2d) is expected, as there is little excess kinetic energy given to the electrons once they have been excited to the conduction band. Note that the  $T_e$  in Fig. 2d is slightly higher than the room temperature value of 294 K, and is the

consequence of not taking into account the transient change in the reflection<sup>32</sup>.

**Transient changes of carriers and excitons.** Next we analyze data over the entire spectral range to extract the other parameters, at each time delay. After photoexcitation, a transient change in the bandgap results from BGR and state-filling, which coexist and compete with each other<sup>33</sup>. Here we introduce a photoinduced change in bandgap ( $\Delta E_g$ ) to account for BGR, and insert a  $(1 - f_{\text{FD}})^2$  factor to account for state-filling effects in both the CB

(for electrons) and VB (for holes), where  $f_{\text{FD}}$  is the Fermi-Dirac distribution function. The CC term is given by

$$\begin{aligned} \Delta A_{\text{CC}}(\hbar\omega) &= A'_{\text{CC}}(E'_b, E'_g, \hbar\omega)(1 - f_{\text{FD}})^2 - A_{\text{CC}}(\hbar\omega) \\ &= f_1 A_1 \frac{2\pi\sqrt{E'_b}}{\hbar\omega} \frac{1}{\Gamma} \int_{E'_g}^{\infty} \text{sech}\left(\frac{\hbar\omega - E}{\Gamma}\right) \frac{\xi(\hbar\omega - E'_g)}{1 - \exp\left(-2\pi\sqrt{\frac{E'_b}{E - E'_g}}\right)} dE \\ &\quad \times \left(1 - \frac{1}{1 + \exp\left(\frac{\hbar\omega - E'_g}{k_B T_e}\right)}\right)^2 - A_1 \frac{2\pi\sqrt{E_b}}{\hbar\omega} \frac{1}{\Gamma} \int_{E_g}^{\infty} \text{sech}\left(\frac{\hbar\omega - E}{\Gamma}\right) \\ &\quad \times \frac{\xi(\hbar\omega - E_g)}{1 - \exp\left(-2\pi\sqrt{\frac{E_b}{E - E_g}}\right)} dE, \end{aligned} \quad (5)$$

where  $E'_b \equiv E_b + \Delta E_b$ ,  $E'_g \equiv E_g + \Delta E_g$ ,  $f_1$  accounts for the photoinduced change in the transition dipole moment embedded in  $A_1$  ( $f_1$  is found to be  $\sim 1$  after pump in our fitting, so we fix  $f_1 = 1$ ), and  $(1 - f_{\text{FD}})^2$  accounts for occupied transitions by carriers, due to the Pauli exclusion principle and characterized by the quasi-Fermi energy  $E_f^q$  and the carrier temperature  $T_e$ . Equation (5) assumes (1) the electron and hole effective masses are nearly the same, (2) a negligible photoinduced change in the nonparabolic parameter  $R$ , and (3)  $T_e \approx T_h$ , where  $T_h$  is the temperature of holes.

Next we consider the EC term. Considering the changes in  $E_b$ ,  $\Gamma$ , and  $E_g$  after photoexcitation, the photoinduced change in the EC term can be expressed as

$$\begin{aligned} \Delta A_{\text{EC}}(\hbar\omega) &= f_2 A'_{\text{EC}}(E'_b, E'_g, \Gamma', \hbar\omega) - A_{\text{EC}}(\hbar\omega) \\ &= f_2 A_2 \frac{2\pi\sqrt{E'_b}}{\hbar\omega} \frac{1}{\Gamma'} \sum_{j=1}^7 \frac{2E'_b}{j^3} \text{sech}\left(\frac{\hbar\omega - E'_g + \frac{E'_b}{j^2}}{\Gamma'}\right) \\ &\quad - A_2 \frac{2\pi\sqrt{E_b}}{\hbar\omega} \frac{1}{\Gamma} \sum_{j=1}^7 \frac{2E_b}{j^3} \text{sech}\left(\frac{\hbar\omega - E_g + \frac{E_b}{j^2}}{\Gamma}\right), \end{aligned} \quad (6)$$

where  $\Gamma' \equiv \Gamma + \Delta\Gamma$ , and  $f_2$  is the prefactor that accounts for the photoinduced change in exciton oscillator strength<sup>31</sup>, which we will show later to be a strong function of pump fluence. The prefactors  $A_1$  and  $A_2$  are fixed values that are obtained from the fitting of the steady-state absorption spectrum earlier, as given in Eq. (2) and Eq. (3).

Combining both the CC and EC terms, we then fit the TA data  $\Delta A(\hbar\omega)$  to

$$\Delta A(\hbar\omega) = \Delta A_{\text{CC}}(\hbar\omega) + \Delta A_{\text{EC}}(\hbar\omega). \quad (7)$$

During the fitting, we found that  $E_f^q$  and  $T_e$  are dependent on each other, i.e., we can find different sets of ( $E_f^q$ ,  $T_e$ ) values that can fit the data equally well (see Supplementary Note 2). This is a consequence of the fact that  $T_e$  and  $E_f^q$  appear in the FD term, and *only* the FD term, via the exponent in Eq. (5), and that  $E_f^q$  will adjust itself depending on the value of  $T_e$ , to yield identical fits. To overcome the problem, since we have obtained  $T_e$  from the MB fits to the normalized  $\Delta A(\hbar\omega)$  at high photon energies, we fix  $T_e$  (extracted from the MB fits in Eq. (4)) to obtain  $E_f^q$  in the fits to Eq. (7). In Eq. (7), by fixing the parameters  $T_e$ ,  $E_g$ ,  $E_b$ , and  $\Gamma$ , the fitting parameters are therefore  $\Delta E_g$ ,  $\Delta E_b$ ,  $\Delta\Gamma$ ,  $E_f^q$  and  $f_2$ . We then plot  $\Delta A_{\text{CC}}(\hbar\omega)$  and  $\Delta A_{\text{EC}}(\hbar\omega)$ , separately, to visualize the carrier (CC) and exciton (EC) terms at each time delay.

Figure 3 shows the CC and EC terms under 400-nm excitation at selected time delays. At 0.5 ps, the bleaching shows a sharp onset at 1.63 eV and a very long high-energy tail. From Fig. 3b, c, we see that the sharp bleaching onset is contributed by both CC and EC terms, while the high-energy tail can be attributed to the

state-filling of hot carriers described by the FD distribution. After several picoseconds, the bleaching dip contributed by carriers moves towards lower-energy states as the carriers lose energy while cascading down to the bandedge, i.e. carrier cooling. At the same time, the carrier bleaching amplitude near the bandedge becomes larger, suggesting the predominance of bandedge transitions (to both carrier and excitonic levels), which is the result of a large number of carriers near the bandedge. At long time delays (Fig. 3e), as carriers keep cooling down to bandedge, the bleaching contributed by carriers moves to even lower energies in the band but the bleaching amplitude decreases with time delay, indicative of a smaller carrier number due to carrier recombination. The EC term does not merely show the change in amplitude, but also in the linewidth and energies of lowest excitonic transitions, which we can recognize from the dip position, as shown in Fig. 3c and f.

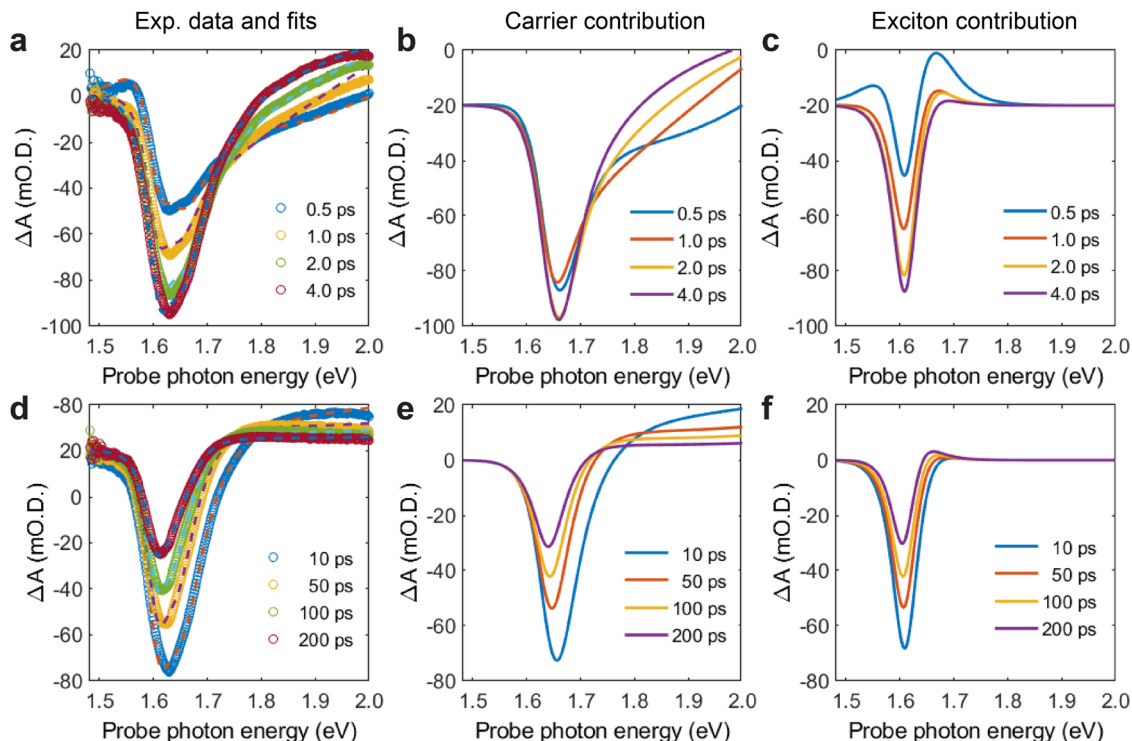
### Quasi-Fermi energy and unusual bandgap renormalization.

From the  $\Delta A$  fittings, we extracted the quasi-Fermi energy  $E_f^q$  under 400-nm and 770-nm photoexcitation, as shown in Fig. 4(a) and (b), respectively. For 400-nm excitation (Fig. 4(a)),  $E_f^q$  increases from  $\sim 1.4$  to 1.6 eV within the first  $\sim 2$  ps. This increase is consistent with more electrons being promoted to the conduction band. Thereafter,  $E_f^q$  decreases slowly to  $\sim 1.55$  eV at 1 ns, suggesting that even after 1 ns, there is still a significant electron population at the conduction band minimum. On the other hand, for 770-nm excitation shown in Fig. 4(b), the extracted  $E_f^q$  remains at  $\sim 1.52$  eV throughout (see Supplementary Note 3 for detailed fittings). This is consistent with the very fast ( $< 0.5$  ps timescale) and resonant absorption of the pump photons by the valence band electrons to the conduction band minimum.

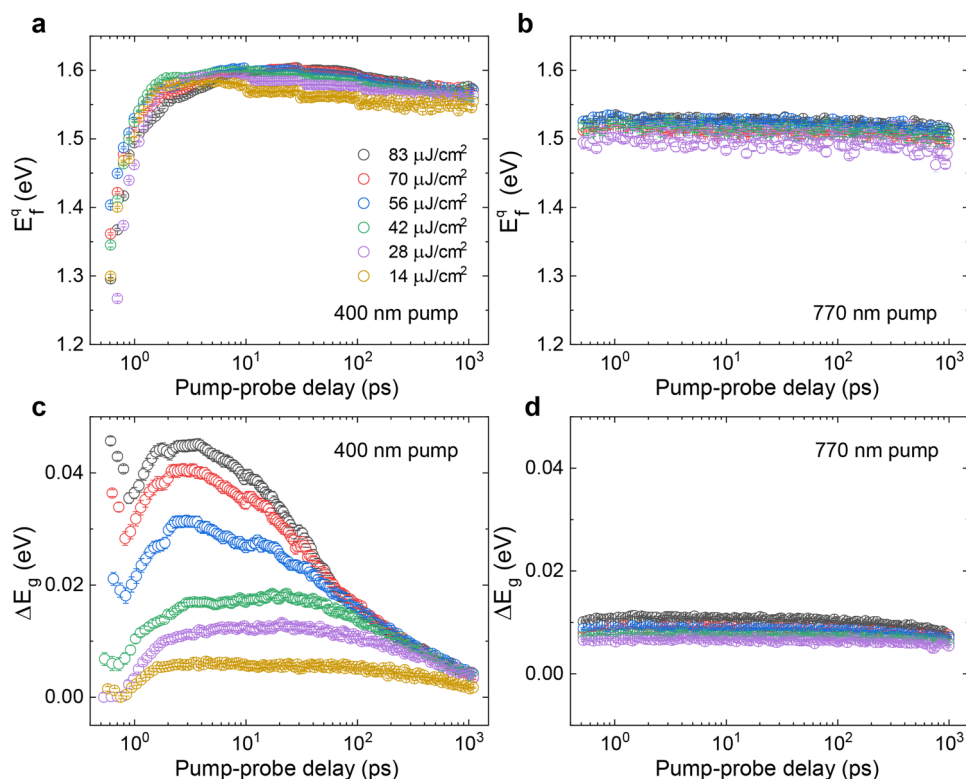
In traditional semiconductors, such as a heavily Sn-doped  $\text{In}_2\text{O}_3$ , the optical bandgap increases with carrier density  $N^{34}$ . This bandgap widening is the combined effect of Burstein-Moss effect and bandgap renormalization, in which the latter contributes to bandgap reduction<sup>34,35</sup>. Walsh et al. later revealed that the nonparabolic nature of the conduction band is a key factor of this renormalization<sup>33</sup>. In inorganic semiconductors such as ZnO nanocrystals, the bandgap decreases with increasing lattice temperature<sup>36</sup>. However, lead halide perovskites exhibit an atypical temperature dependence of bandgap—the bandgap increases with increasing temperature<sup>20,37</sup>. This temperature dependence of the bandgap in  $\text{MAPbI}_3$  is attributed to both thermal expansion and electron-phonon interactions, of which the former predominantly contributes to the BGR<sup>38</sup>. This temperature dependence of the fundamental gap makes the sign of photoinduced change in bandgap uncertain—it is not entirely certain that BGR necessarily results in a bandgap reduction in the perovskites.

Figure 4(c) and (d) show the time evolution of  $\Delta E_g$  under 400-nm pump and 770-nm pump. In contrast to previous TA works<sup>4,21,22</sup>, our extracted  $\Delta E_g$  is positive at all time delays for all pump fluences, implying that the bandgap increases after photoexcitation. This is consistent with the temperature dependence of the bandgap<sup>20,37</sup>.

**Carrier and exciton dynamics.** After photoexcitation, part of the conduction band (valence band) is occupied by photoexcited electrons (holes). These filled states lead to ground-state bleaching. In past reports, the time evolution of the carrier density was obtained via time-resolved terahertz spectroscopy (TRTS)<sup>39,40</sup>. Here we show that TA data can do the same, and thus serve as a complimentary check to the TRTS results. With the assumption that the electron density is equal to the hole density, the electron density  $N_e$  can be a measure of carrier density  $N$ , that is calculated from the extracted fitting parameters  $E_g$ ,  $E_b$ ,  $E_f^q$ , and  $T_e$  via the



**Fig. 3 Disentanglement of carrier and exciton components.** Transient absorption (TA) spectra  $\Delta A(\hbar\omega)$  for experimental data (circles) and fits (dashed lines) (a–c) at short time delays and (d–f) long time delays for 400-nm pump. Carrier contribution [CC] term and exciton contribution [EC] term are shown in b, e and c, f, respectively.  $\Delta A(\hbar\omega)$  is the transient change of the absorption spectrum at certain pump-probe time delays with respect to the steady-state one.  $\hbar$  is the reduced Planck constant and  $\omega$  is the photon frequency. O.D. is the optical density, as defined in Fig. 1.



**Fig. 4 Extracted parameters from the fitting.** Photoinduced change in quasi-Fermi energy  $E_f^q$  (a, b) and bandgap  $\Delta E_g$  (c, d).  $\Delta E_g$  is defined as the energy difference of bandgap  $E_g$  between after- and before- photoexcitation. All  $\Delta E_g$  are found to be positive. Errors of the parameters are standard error that is determined by calculating the 95% confidence interval, based on residual values and Jacobian matrix obtained from the fits to Eq. (7).

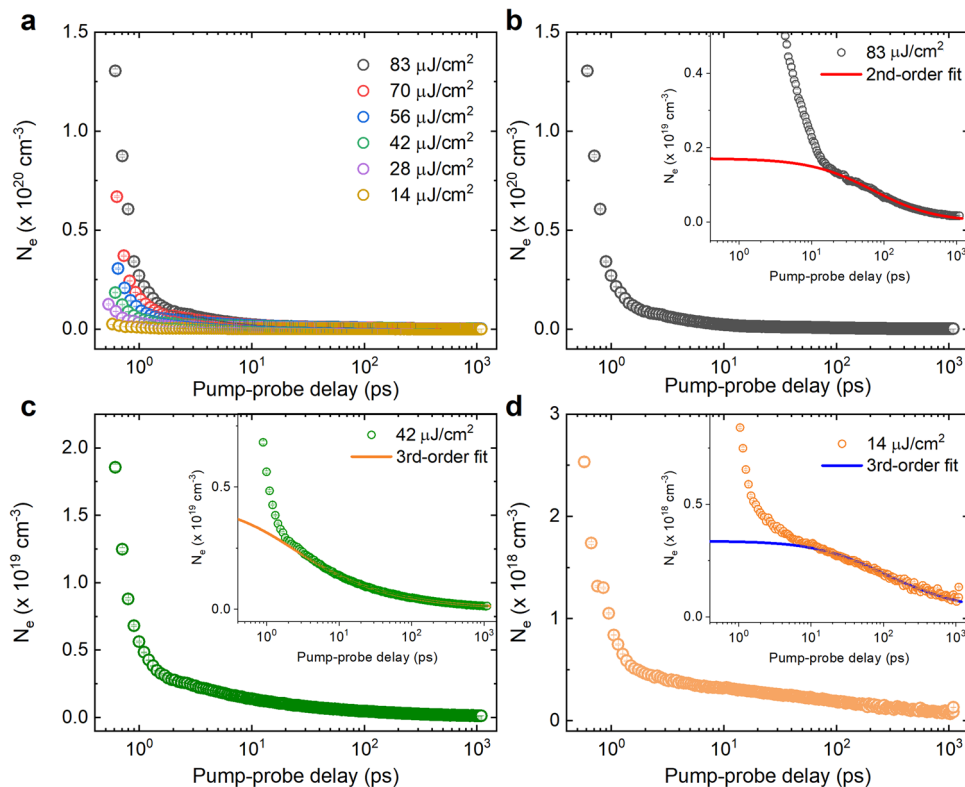


**Fig. 5 Photogenerated electron density  $N_e$  and its dynamics.** **a** Time evolution of  $N_e$  under 400-nm pump with different pump fluences. **b**  $N_e$  and its second-order rate equation fit (zooming in the inset) for  $83 \mu\text{J}/\text{cm}^2$  within 20–1000 ps. **c**, **d**  $N_e$  and its third-order rate equation fit in the inset for 42 and  $14 \mu\text{J}/\text{cm}^2$  within 20–1000 ps. The fitted curves in the insets are extrapolated to short time delays. Error of  $N_e$  is calculated via Eq. (8) according to propagation of error.

formula  $N_e = \int_{E_g}^{\infty} D_c(\hbar\omega) f_{\text{FD}} d\hbar\omega$ , where  $D_c(\hbar\omega)$  is the density of states of conduction band<sup>4</sup>. The full expression is

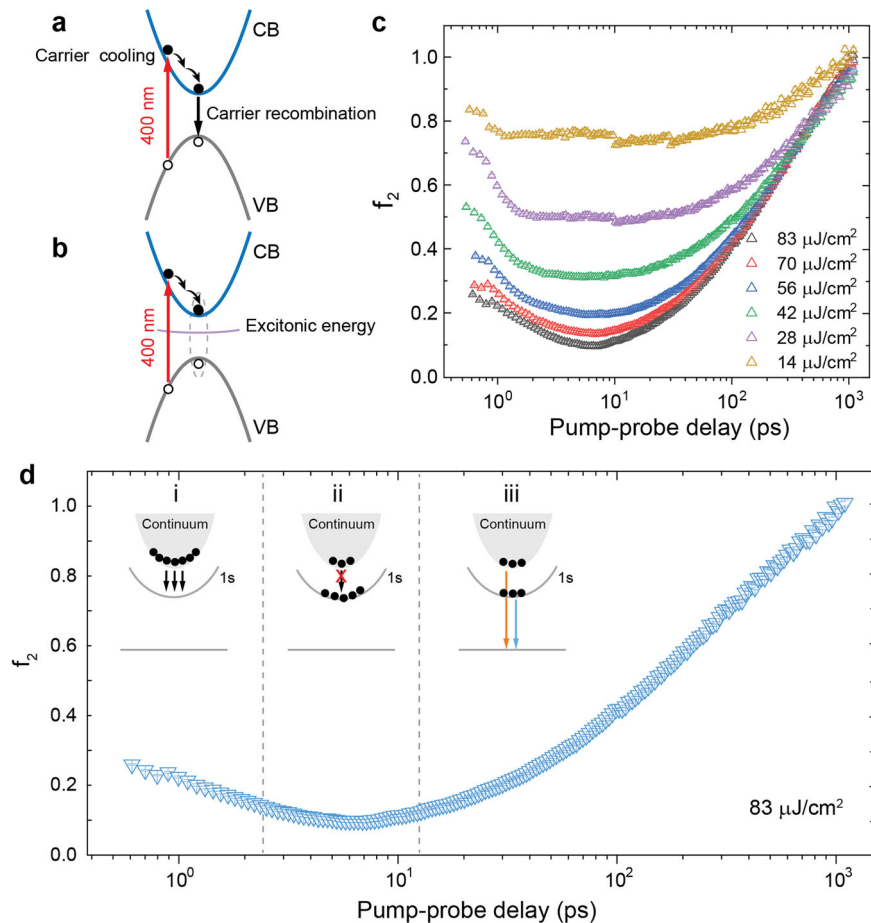
$$N_e = \int_{E_g}^{\infty} \frac{1}{2\pi^2} \left( \frac{2m_{\text{eff}}}{\hbar^2} \right)^{\frac{3}{2}} \sqrt{E - E_g} \frac{\xi(E - E_g)}{1 + \exp((E - E_g)/k_B T)} dE \quad (8)$$

Figure 5a shows the obtained time evolution of electron densities  $N_e$  for different 400-nm pump fluences. The highest pump fluence of  $83 \mu\text{J}/\text{cm}^2$  yields a carrier density on the order of  $10^{20} \text{cm}^{-3}$  at short time delay. The values of  $N_e$  at smaller pump fluences have the same order of magnitude as that of  $\text{CH}_3\text{NH}_3\text{PbI}_3$  under 400-nm pump and similar pump fluences using time-resolved THz spectroscopy<sup>40</sup>. By modeling the decay of the electron densities  $N_e$  by the rate equation given by  $-dN(t)/dt = k_1N + k_2N^2 + k_3N^3$ , we identified the carrier recombination process for different pump fluences (see Supplementary Note 4) and found a pump-fluence-dependent carrier recombination mechanism, that is, the carrier recombination process undergoes a transition from second-order for high-fluence excitation ( $\geq 56 \mu\text{J}/\text{cm}^2$ ) to third-order for low-fluence excitation ( $\leq 42 \mu\text{J}/\text{cm}^2$ ). The insets of Fig. 5b, c and d show the fitting curves of  $83 \mu\text{J}/\text{cm}^2$  for a second-order process and of 42 and  $14 \mu\text{J}/\text{cm}^2$  for a third-order process in the range of 20–1000 ps. A change of recombination kinetics has been previously reported in  $\text{CH}_3\text{NH}_3\text{PbI}_3$  perovskite film, that is from two-body recombination at room temperature to three-body recombination at low temperatures<sup>40</sup>. Though not in the sense of lattice temperature, the higher pump fluences yield higher carrier temperatures, which might explain the similar change of the recombination kinetics for pump fluence and temperature. The extrapolated fitting curve to shorter time delays (see Fig. 5b) underestimates the experimental electron density.

This underestimation was also observed in a time-resolved THz spectroscopy work of FCPIB<sup>24</sup>. This discrepancy suggests the existence of additional decay channels for the carriers at early time delays, which we attribute to exciton formation, as will be justified later in our discussion.

After obtaining the carrier and exciton dynamics from our fits, we now provide a physical picture of what happens to the photogenerated carriers, as shown in Fig. 6. After 400-nm photoexcitation, electrons are generated in the CB. These electrons then cascade down to the bottom of the CB via electron–phonon interactions. At the CB minimum, there are two possible paths for the electrons to take: (1) some electrons recombine with holes in the VB (see Fig. 6a) via radiative or non-radiative recombination—the recombination order (second or third) depends on the pump fluence; (2) other electrons bind with holes, forming excitons in the lower-lying excitonic levels via phonon emission (see Fig. 6b). Path (2) accounts for the discrepancy between the experimental  $N_e$  and theoretical  $N_e$  extrapolated from the carrier recombination curve (solid lines in Fig. 5b–d).

The physical picture above is substantiated by the time evolution of the exciton oscillator strength  $f_2$ . Strictly speaking,  $f_2$  is the ratio of exciton oscillator strength after photoexcitation to that before photoexcitation, and so is a measure of the excitonic state-filling effect. The (bound) electron and hole levels that are already filled will not be available for subsequent electrons in the CB (and holes in the VB) to fill them, so a small  $f_2$  implies a large excitonic state-filling effect. Taking the highest-fluence data of  $83 \mu\text{J}/\text{cm}^2$  as an example, at the shortest time delays ( $< 1$  ps),  $f_2$  is already 0.25 (see Fig. 6d), i.e. much less than 1, indicating a rapid filling of the excitonic states (see region  $i$  in Fig. 6d) and a concurrent rapid decay of  $N_e$  (see Fig. 5a). Up till  $\sim 10$  ps,  $f_2$



**Fig. 6 Fate of photogenerated carriers.** Two possible paths of carriers to **a** recombine with holes in the valence band, involving (or without involving) a third carrier, and **b** bind with holes, forming excitons in the excitonic levels. CB and VB mean conduction band and valence band, respectively. **c** The time evolution of  $f_2$  at different pump fluences. **d** The  $f_2$  evolution for 83  $\mu\text{J}/\text{cm}^2$ . The inset illustrates three stages of relaxation between the free carrier band (continuum) and the exciton level (1s level) (denoted by black arrows). The red "X" denotes the transition has been forbidden because of excitonic state-filling effect. The orange and blue arrows denote the carrier recombination and exciton decay, respectively. Errors of  $f_2$  are standard error that is determined by calculating the 95% confidence interval, based on residual values and Jacobian matrix obtained from the fits to Eq. (7).

continues to decrease, resulting from more excitonic states being filled, and reaches a minimum value of  $\sim 0.1$  at  $\sim 10$  ps (see region *ii* in Fig. 6d). At  $\sim 10$  ps,  $f_2$  starts to increase, corresponding to the gradual "vacating" of the previously-filled excitonic states either via excitonic recombination or excitonic dissociation, while carrier recombination becomes more and more dominant (see region *iii* in Fig. 6d). From  $\sim 10$  ps to  $\sim 1$  ns, the quenched  $f_2$  starts to recover and approaches unity. At  $\sim 1$  ns, the other fitting parameters also return to their pre-photoexcitation values (see Supplementary Fig. 9).

At lower pump fluences (e.g., 14 and 28  $\mu\text{J}/\text{cm}^2$  in Fig. 6c),  $f_2$  is closer to 1, and stays at a constant value for a longer period of time after photoexcitation. The corresponding  $N_e$  is smaller in magnitude, and does not manifest a sharp upturn at the shortest time delays (see Fig. 5a). Nonetheless the general trend persists. Our physical picture of the fate of the photogenerated carriers are thus confirmed by the time evolution of  $N_e$  (with its rate equation fits) and  $f_2$ . The very long (nanosecond) timescale of our carrier dynamics is also consistent with polaron formation as reported in other reports<sup>24,41,42</sup>. At high pump fluences and short time delays, the excitons are more strongly depleted, which suggests the use of a high pump fluence as a knob to tune the exciton populations and hence the carrier-to-exciton conversion efficiencies. Since the binding energy of the excitons has to be overcome in order to

obtain free charge carriers and to make the current flow, a higher pump fluence below the damage threshold may benefit the performance of perovskites in photovoltaic applications.

## Conclusions

We have investigated the carrier and exciton dynamics via transient absorption spectroscopy in FCPIB perovskites. By successfully fitting both the steady-state and transient absorption spectra with a nonparabolic band structure, we revealed a positive photoinduced change in  $\Delta E_g$ , which is consistent with the anomalous increase of the perovskite bandgap with temperature. From the fitting parameters, we disentangled the time evolutions of carrier density  $N_e$  and exciton oscillator strength  $f_2$ , which enables us to visualize the interesting interplay between carriers and excitons at the bottom of the bands. By fitting carrier density  $N_e$  to the rate equation, we reveal a change of kinetics from a second-order recombination at high pump fluence to a third-order recombination at low fluence. The underestimated  $N_e$  and the decrease of  $f_2$  at short time delay suggest the existence of exciton formation. Furthermore, the time evolution of  $f_2$  provides information on exciton formation, exciton decay and carrier recombination processes, which extends our fundamental understanding of photophysics in the perovskite family.

## Methods

**Sample preparation.**  $\text{FA}_{0.85}\text{Cs}_{0.15}\text{Pb}(\text{I}_{0.97}\text{Br}_{0.03})_3$  thin film was grown in a solution-based method. The perovskite precursor solution was prepared by dissolving the precursors  $\text{FAI}$ ,  $\text{CsI}$ ,  $\text{PbI}_2$ , and  $\text{PbBr}_2$  with respective stoichiometric ratio in a mixed organic solvent system comprising anhydrous  $\text{N,N}$ -dimethylformamide (DMF) and anhydrous dimethyl sulfoxide (DMSO) at the volume ratio of  $\text{DMF:DMSO} = 4:1$ . The  $z$ -cut substrate was cleaned with Hellmanex II solution (1% v/v), deionized water, acetone, and isopropyl alcohol in an ultrasonic bath for 15 min, and then treated with an air plasma treatment for 15 min and subsequently transferred to a nitrogen glove box for the deposition of perovskite films. The perovskite film was prepared by spin-coating the perovskite solution (0.5 mol/L) on quartz substrate at 1000 r.p.m. for the first 10 s and 4000 r.p.m. for the following 30 s. Chlorobenzene (200  $\mu\text{L}$ ) was dripped fast on the sample surface at 15 s before finishing the spin-coating. Immediately, the substrate was placed on a hotplate for thermal annealing at 80 °C for 5 min, then 120 °C for 5 min, and then 180 °C for 30 min.

## Steady-state absorption spectra measurement: Ellipsometer transmission mode.

The steady-state absorption spectrum was measured using variable angle spectroscopic ellipsometry (VASE) in the transmission mode. The film sample was illuminated by a halogen lamp and the transmitted light was then resolved by a monochromator and collected by a photomultiplier.

**Transient absorption measurement.** Transient absorption spectra were measured using a commercial spectroscopy (Helios Fire, Ultrafast Systems, Inc.). The 400-nm pump pulses are doubled from a 800-nm laser (Coherent Legend elite amplifier, 800 nm, 35 fs, 1 kHz, 4 mJ) using a beta barium borate (BBO) crystal. White-light continuum source was produced by focusing the 800-nm laser pulses on a sapphire plate. We first excite the sample with a 400-nm pulse, then use a white-light pulse to measure the photoinduced changes in the absorption of the sample.

## Data availability

The data that support the findings of this study are available from the corresponding author upon reasonable request.

## Code availability

The code that supports the findings of this study are available from the corresponding author upon reasonable request.

Received: 11 January 2022; Accepted: 5 July 2022;

Published online: 19 July 2022

## References

- De Wolf, S. et al. Organometallic halide perovskites: sharp optical absorption edge and its relation to photovoltaic performance. *J. Phys. Chem. Lett.* **5**, 1035–1039 (2014).
- Xiao, Z., Song, Z. & Yan, Y. From lead halide perovskites to lead-free metal halide perovskites and perovskite derivatives. *Adv. Mater.* **31**, 1803792 (2019).
- Xing, G. et al. Long-range balanced electron-and hole-transport lengths in organic-inorganic  $\text{CH}_3\text{NH}_3\text{PbI}_3$ . *Science* **342**, 344–347 (2013).
- Yang, Y. et al. Observation of a hot-phonon bottleneck in lead-iodide perovskites. *Nat. Photon.* **10**, 53 (2016).
- Jeng, J. et al.  $\text{CH}_3\text{NH}_3\text{PbI}_3$  perovskite/fullerene planar-heterojunction hybrid solar cells. *Adv. Mater.* **25**, 3727–3732 (2013).
- Ponseca Jr., C. S. et al. Organometal halide perovskite solar cell materials rationalized: ultrafast charge generation, high and microsecond-long balanced mobilities, and slow recombination. *J. Am. Chem. Soc.* **136**, 5189–5192 (2014).
- Sun, S. et al. The origin of high efficiency in low-temperature solution-processable bilayer organometal halide hybrid solar cells. *Energy Environ. Sci.* **7**, 399–407 (2014).
- Saliba, M. et al. Incorporation of rubidium cations into perovskite solar cells improves photovoltaic performance. *Science* **354**, 206–209 (2016).
- Green, M. A. et al. Solar cell efficiency tables (version 49). *Prog. Photovolt.* **25**, 3–13 (2017).
- McMeekin, D. P. et al. A mixed-cation lead mixed-halide perovskite absorber for tandem solar cells. *Science* **351**, 151–155 (2016).
- Liang, D. et al. Color-pure violet-light-emitting diodes based on layered lead halide perovskite nanoplates. *ACS Nano* **10**, 6897–6904 (2016).
- Kim, Y. et al. Highly efficient light-emitting diodes of colloidal metal-halide perovskite nanocrystals beyond quantum size. *ACS Nano* **11**, 6586–6593 (2017).

- Xing, G. et al. Low-temperature solution-processed wavelength-tunable perovskites for lasing. *Nat. Mater.* **13**, 476–480 (2014).
- Yakunin, S. et al. Low-threshold amplified spontaneous emission and lasing from colloidal nanocrystals of caesium lead halide perovskites. *Nat. Commun.* **6**, 1–9 (2015).
- Lee, J.-W. et al. Formamidinium and cesium hybridization for photo-and moisture-stable perovskite solar cell. *Adv. Energy Mater.* **5**, 1501310 (2015).
- Yi, C. et al. Entropic stabilization of mixed A-cation  $\text{ABX}_3$  metal halide perovskites for high performance perovskite solar cells. *Energy Environ. Sci.* **9**, 656–662 (2016).
- Li, Z. et al. Stabilizing perovskite structures by tuning tolerance factor: formation of formamidinium and cesium lead iodide solid-state alloys. *Chem. Mater.* **28**, 284–292 (2016).
- Lin, Y.-H. et al. A piperidinium salt stabilizes efficient metal-halide perovskite solar cells. *Science* **369**, 96–102 (2020).
- Yang, W. S. et al. Iodide management in formamidinium-lead-halide-based perovskite layers for efficient solar cells. *Science* **356**, 1376–1379 (2017).
- D'Innocenzo, V. et al. Excitons versus free charges in organo-lead tri-halide perovskites. *Nat. Commun.* **5**, 1–6 (2014).
- Fu, J. et al. Hot carrier cooling mechanisms in halide perovskites. *Nat. Commun.* **8**, 1–9 (2017).
- Mondal, A. et al. Ultrafast exciton many-body interactions and hot-phonon bottleneck in colloidal cesium lead halide perovskite nanocrystals. *Phys. Rev. B* **98**, 115418 (2018).
- Manser, J. S. & Kamat, P. V. Band filling with free charge carriers in organometal halide perovskites. *Nat. Photon.* **8**, 737–743 (2014).
- Zhao, D. et al. Monitoring electron-phonon interactions in lead halide perovskites using time-resolved THz spectroscopy. *ACS Nano* **13**, 8826–8835 (2019).
- Jiang, S. et al. Pressure-dependent polymorphism and band-gap tuning of methylammonium lead iodide perovskite. *Angew. Chem.* **128**, 6650–6654 (2016).
- Elliott, R. J. Intensity of optical absorption by excitons. *Phys. Rev.* **108**, 1384 (1957).
- Yang, Y. et al. Comparison of recombination dynamics in  $\text{CH}_3\text{NH}_3\text{PbBr}_3$  and  $\text{CH}_3\text{NH}_3\text{PbI}_3$  perovskite films: influence of exciton binding energy. *J. Phys. Chem. Lett.* **6**, 4688–4692 (2015).
- Saba, M. et al. Correlated electron-hole plasma in organometal perovskites. *Nat. Commun.* **5**, 1–10 (2014).
- Sestu, N. et al. Absorption F-sum rule for the exciton binding energy in methylammonium lead halide perovskites. *J. Phys. Chem. Lett.* **6**, 4566–4572 (2015).
- Dresselhaus, M. S. *Solid State Physics Part II Optical Properties of Solids. Lecture Notes* (Massachusetts Institute of Technology, 2001).
- Huang, D., Chyi, J.-I. & Morkoc, H. Carrier effects on the excitonic absorption in GaAs quantum-well structures: Phase-space filling. *Phys. Rev. B* **42**, 5147 (1990).
- Price, M. B. et al. Hot-carrier cooling and photoinduced refractive index changes in organic-inorganic lead halide perovskites. *Nat. Commun.* **6**, 1–8 (2015).
- Walsh, A., Da Silva, J. L. F. & Wei, S. Origins of band-gap renormalization in degenerately doped semiconductors. *Phys. Rev. B* **78**, 075211 (2008).
- Hamberg, I., Granqvist, C. G., Berggren, K.-F., Sernelius, B. E. & Engström, L. Band-gap widening in heavily Sn-doped  $\text{In}_2\text{O}_3$ . *Phys. Rev. B* **30**, 3240 (1984).
- Berggren, K.-F. & Sernelius, B. E. Band-gap narrowing in heavily doped many-valley semiconductors. *Phys. Rev. B* **24**, 1971 (1981).
- Li, J. W. et al. Bandgap modulation in ZnO by size, pressure, and temperature. *J. Phys. Chem. C* **114**, 13370–13374 (2010).
- Foley, B. J. et al. Temperature dependent energy levels of methylammonium lead iodide perovskite. *Appl. Phys. Lett.* **106**, 243904 (2015).
- Francisco-López, A. et al. Equal footing of thermal expansion and electron-phonon interaction in the temperature dependence of lead halide perovskite band gaps. *J. Phys. Chem. Lett.* **10**, 2971–2977 (2019).
- Wehrenfennig, C., Eperon, G. E., Johnston, M. B., Snaith, H. J. & Herz, L. M. High charge carrier mobilities and lifetimes in organolead trihalide perovskites. *Adv. Mater.* **26**, 1584–1589 (2014).
- La-o-vorakiat, C. et al. Elucidating the role of disorder and free-carrier recombination kinetics in  $\text{CH}_3\text{NH}_3\text{PbBr}_3$  perovskite films. *Nat. Commun.* **6**, 1–8 (2015).
- Miyata, K., Atallah, T. L. & Zhu, X. Lead halide perovskites: crystal-liquid duality, phonon glass electron crystals, and large polaron formation. *Sci. Adv.* **3**, e1701469 (2017).
- Cinquanta, E. et al. Ultrafast thz probe of photoinduced polarons in lead-halide perovskites. *Phys. Rev. Lett.* **122**, 166601 (2019).

## Acknowledgements

E.E.M.C. acknowledges support from Singapore Ministry of Education (MOE) AcRF Tier 2 grant (No. MOE2019-T2-1-097). H.S. acknowledges support from funding AME-IRG-



A20E5c0083. Y.M.L. acknowledges financial support from Ministry of Education (MOE-T2-1-085). Work at Los Alamos was carried out under the auspices of the U.S. Department of Energy (DOE) National Nuclear Security Administration under Contract No. 89233218CNA000001, and was supported by LANL LDRD Program. This work was supported in part by the Center for Integrated Nanotechnologies, a U.S. DOE BES user facility.

### Author contributions

E.E.M.C. and D.M.Z. conceived and designed the experiment. H.W.H. and B.B.C. from Y.M.L.'s group prepared the sample. X.X.C. from H.D.S.'s group performed steady-state absorption spectrum measurement. Q.C. performed the transient absorption experiments. Q.C. and D.B. prepared the figures for the manuscript. Q.C., D.B., D.M.Z., E.E.M.C., and J.X.Z. interpreted the data and wrote the manuscript with the input from all authors.

### Competing interests

The authors declare no competing interests.

### Additional information

**Supplementary information** The online version contains supplementary material available at <https://doi.org/10.1038/s42005-022-00966-4>.

**Correspondence** and requests for materials should be addressed to Daming Zhao or Elbert E. M. Chia.

**Peer review information** *Communications Physics* thanks the anonymous reviewers for their contribution to the peer review of this work. Peer reviewer reports are available.

**Reprints and permission information** is available at <http://www.nature.com/reprints>

**Publisher's note** Springer Nature remains neutral with regard to jurisdictional claims in published maps and institutional affiliations.



**Open Access** This article is licensed under a Creative Commons Attribution 4.0 International License, which permits use, sharing, adaptation, distribution and reproduction in any medium or format, as long as you give appropriate credit to the original author(s) and the source, provide a link to the Creative Commons license, and indicate if changes were made. The images or other third party material in this article are included in the article's Creative Commons license, unless indicated otherwise in a credit line to the material. If material is not included in the article's Creative Commons license and your intended use is not permitted by statutory regulation or exceeds the permitted use, you will need to obtain permission directly from the copyright holder. To view a copy of this license, visit <http://creativecommons.org/licenses/by/4.0/>.

© The Author(s) 2022